

# Event patterns extracted from transverse momentum and rapidity spectra of $Z$ bosons and quarkonium states produced in $pp$ and Pb-Pb collisions at LHC

Ya-Hui Chen<sup>a</sup>, Fu-Hu Liu<sup>a,1</sup>, and Roy A. Lacey<sup>b,2</sup>

<sup>a</sup>*Institute of Theoretical Physics, Shanxi University, Taiyuan, Shanxi 030006, China*

<sup>b</sup>*Departments of Chemistry & Physics, Stony Brook University, Stony Brook, NY 11794, USA*

**Abstract:** Transverse momentum ( $p_T$ ) and rapidity ( $y$ ) spectra of  $Z$  bosons and quarkonium states (some charmonium  $c\bar{c}$  mesons such as  $J/\psi$  and  $\psi(2S)$ , and some bottomonium  $b\bar{b}$  mesons such as  $\Upsilon(1S)$ ,  $\Upsilon(2S)$ , and  $\Upsilon(3S)$ ) produced in proton-proton ( $pp$ ) and lead-lead (Pb-Pb) collisions at the large hadron collider (LHC) are uniformly described by a hybrid model of two-component Erlang distribution for  $p_T$  spectrum and two-component Gaussian distribution for  $y$  spectrum. The former distribution results from a multisource thermal model, and the latter one results from the revised Landau hydrodynamic model. The modelling results are in agreement with the experimental data measured in  $pp$  collisions at center-of-mass energies  $\sqrt{s} = 2.76$  and 7 TeV, and in Pb-Pb collisions at center-of-mass energy per nucleon pair  $\sqrt{s_{NN}} = 2.76$  TeV. Based on the parameter values extracted from  $p_T$  and  $y$  spectra, the event patterns (particle scatter plots) in two-dimensional  $p_T$ - $y$  space and in three-dimensional velocity space are obtained.

**Keywords:** Transverse momentum spectrum, rapidity spectrum, event pattern

**PACS:** 12.38.Mh, 25.75.Dw, 24.10.Pa

## 1 Introduction

High energy nucleus-nucleus collisions at the relativistic heavy ion collider (RHIC) [1–4] and large hadron collider (LHC) [5–8] provide excellent environment and condition of high temperature and density [9], where a new state of matter, namely the quark-gluon plasma (QGP) [10–12], is expected to form and to live for a very short time. It is regretful that the QGP cannot be directly measured in experiments due to its very short lifetime. Instead, to understand the formation and properties of QGP, the distribution laws of final-state particles are studied. Because of the complexities and difficulties in experiments, the observables are limited. To obtain more information from limited observables, we need more modelling and theoretical analyses.

Generally, an interacting system of nucleus-nucleus collisions undergoes a few stages which include, but are not limited to, the scattering, color glass condensate, thermaliza-

---

<sup>1</sup>E-mail: fuhuliu@163.com; fuhuliu@sxu.edu.cn

<sup>2</sup>E-mail: Roy.Lacey@Stonybrook.edu

tion, hadronization, chemical equilibrium and freeze-out, kinetic equilibrium and freeze-out. The distribution laws of final-state particle transverse momenta and rapidities reflect the situation of interacting system at the stage of kinetic freeze-out, while the feed-down corrected yields and the ratios of those yields of different particles reflect the situation at the stage of chemical freeze-out. Based on the descriptions of transverse momentum ( $p_T$ ) and rapidity ( $y$ ) spectra, one can extract some information of transverse excitation and longitudinal expansion of interacting system. Thus, other information such as the event pattern (particle scatter plot) in two-dimensional  $p_T$ - $y$  space and three-dimensional velocity space can be extracted from parameters fitted to  $p_T$  and  $y$  spectra [13, 14].

In peripheral nucleus-nucleus collisions, less nucleons take part in the interactions. The most peripheral nucleus-nucleus collisions contain only two nucleons which are from the two collision nuclei respectively. Proton-proton ( $pp$ ) collisions are similar to the most peripheral nucleus-nucleus collisions in the case of neglecting the spectator (cold nuclear) effect. As an input quantity and a basic collision process,  $pp$  collisions can be used to give comparisons with nucleus-nucleus collisions. We are interested in both  $pp$  collisions and lead-lead (Pb-Pb) collisions at the LHC.

To understand the stage of kinetic freeze-out in high energy collisions, we can analyze the  $p_T$  and  $y$  spectra to obtain the probability density functions  $f_{p_T}(p_T)$  for  $p_T$  and  $f_y(y)$  for  $y$ . Nevertheless, these probability density functions cannot directly give us a whole and perceptual picture of the interacting system at the stage of kinetic freeze-out. In fact, a whole and perceptual picture can help us understand the interacting mechanisms in detail. Fortunately, we can use the Monte Carlo method to extract some discrete values of  $p_T$  and  $y$  based on  $f_{p_T}(p_T)$  and  $f_y(y)$ . Other quantities such as energy, momentum components, velocity, and velocity components can be obtained according to some definitions and assumptions. Because  $f_{p_T}(p_T)$  for  $p_T$  and  $f_y(y)$  for  $y$  are based on descriptions of experimental spectra, the extracted discrete values are independent of models.

In this paper, based on a hybrid model of two-component Erlang distribution for  $p_T$  spectrum (which results from a multisource thermal model [15–17]) and two-component Gaussian distribution for  $y$  spectrum (which results from the Landau hydrodynamic model and its revisions [18–26]), we analyze together  $p_T$  and  $y$  spectra of  $Z$  bosons and quarkonium states (some charmonium  $c\bar{c}$  mesons such as  $J/\psi$  and  $\psi(2S)$ , and some bottomonium  $b\bar{b}$  mesons such as  $\Upsilon(1S)$ ,  $\Upsilon(2S)$ , and  $\Upsilon(3S)$ ) produced in  $pp$  collisions at center-of-mass energies  $\sqrt{s} = 2.76$  and 7 TeV, and in Pb-Pb collisions at center-of-mass energy per nucleon pair  $\sqrt{s_{NN}} = 2.76$  TeV. The modelling results are in agreement with the experimental data measured at the LHC. Based on the parameters extracted from  $p_T$  and  $y$  spectra, the event patterns (particle scatter plots) at kinetic freeze-out in two-dimensional  $p_T$ - $y$  space and in three-dimensional velocity space are obtained.

The structure of the present work is as followings. The model and method are shortly described in section 2. Results and discussion are given in section 3. In section 4, we summarize our main observations and conclusions.

## 2 The model and method

Firstly, we need modelling descriptions of  $p_T$  and  $y$  spectra. In the framework of multisource thermal model [15–17], we can obtain an Erlang distribution or a two-, three- or multi-component Erlang distribution to fit  $p_T$  spectrum. According to the model, many ( $m$ ) emission sources which stay at the same excitation state are assumed to form in high energy collisions. Each (the  $i$ -th) source is assumed to contribute to transverse momentum  $p_{Ti}$  by an exponential function

$$f_{p_{Ti}}(p_{Ti}) = \frac{1}{\langle p_{Ti} \rangle} \exp \left( - \frac{p_{Ti}}{\langle p_{Ti} \rangle} \right), \quad (1)$$

where  $\langle p_{Ti} \rangle$  denotes the average value of  $p_{Ti}$ , which results in Eq. (1) to be a probability distribution and  $\int_0^\infty f_{p_{Ti}}(p_{Ti}) dp_{Ti} = 1$ . The  $m$  sources which contribute to  $p_T$  resulting in an Erlang distribution [17]

$$f_{p_T}(p_T) = \frac{p_T^{m-1}}{(m-1)! \langle p_{Ti} \rangle^m} \exp \left( - \frac{p_T}{\langle p_{Ti} \rangle} \right) \quad (2)$$

which is the folding of  $m$  exponential distributions and has the average transverse momentum  $\langle p_T \rangle = m \langle p_{Ti} \rangle$ .

In the case of considering the two-component Erlang distribution, we have

$$f_{p_T}(p_T) = \frac{k_1 p_T^{m_1-1}}{(m_1-1)! \langle p_{Ti} \rangle_1^{m_1}} \exp \left( - \frac{p_T}{\langle p_{Ti} \rangle_1} \right) + \frac{(1-k_1) p_T^{m_2-1}}{(m_2-1)! \langle p_{Ti} \rangle_2^{m_2}} \exp \left( - \frac{p_T}{\langle p_{Ti} \rangle_2} \right) \quad (3)$$

which has the average transverse momentum  $\langle p_T \rangle = k_1 m_1 \langle p_{Ti} \rangle_1 + (1-k_1) m_2 \langle p_{Ti} \rangle_2$ , where  $k_1$  and  $1-k_1$  denote the relative contributions of the first and second components which contribute in the low- and high- $p_T$  regions respectively, and the subscripts 1 and 2 denote the quantities related to the first and second components respectively. Eqs. (2) and (3) are probability distributions which are normalized to 1. When we compare them with experimental data, normalization constant ( $N_{p_T}$ ) which is used to fit the data is needed.

On  $y$  spectrum, we choose the Landau hydrodynamic model and its revisions [18–26] which are called the revised Landau hydrodynamic model in the present work. In the model, the interacting system is described by the hydrodynamics. The  $y$  spectrum can be described by a Gaussian function [25, 26]

$$f_y(y) = \frac{1}{\sqrt{2\pi}\sigma_y} \exp \left[ - \frac{(y-y_C)^2}{2\sigma_y^2} \right], \quad (4)$$

where  $\sigma_y$  denotes the rapidity distribution width and  $y_C$  denotes the mid-rapidity (peak position). In symmetric collisions,  $y_C = 0$  is in the center-of-mass reference frame.

In the case of considering the two-component Gaussian function for  $y$  spectrum, we have

$$f_y(y) = \frac{k_B}{\sqrt{2\pi}\sigma_{yB}} \exp \left[ - \frac{(y-y_B)^2}{2\sigma_{yB}^2} \right] + \frac{1-k_B}{\sqrt{2\pi}\sigma_{yF}} \exp \left[ - \frac{(y-y_F)^2}{2\sigma_{yF}^2} \right], \quad (5)$$

where  $k_B$  ( $1 - k_B$ ),  $y_B$  ( $y_F$ ), and  $\sigma_{yB}$  ( $\sigma_{yF}$ ) denote respectively the relative contribution, peak position, and distribution width of the first (second) component which distributes in the backward (forward) rapidity region. In symmetric collisions such as  $pp$  and Pb-Pb collisions which are considered in the present work, we have  $k_B = 1 - k_B = 0.5$ ,  $y_B = -y_F$ , and  $\sigma_{yB} = \sigma_{yF}$ . As probability distributions, Eqs. (4) and (5) are normalized to 1. When we compare them with experimental data, a normalization constant ( $N_y$ ) which is used to fit the data is needed.

*Secondly*, we need discrete values of  $p_T$  and  $y$ . The related calculation is performed by a Monte Carlo method. Let  $r_i$ ,  $r_{1i}$ ,  $r_{2i}$ , and  $R_{1,2,\dots,7}$  denote random numbers in  $[0,1]$ . Eqs. (2)–(5) results in

$$p_T = -\langle p_{Ti} \rangle \sum_{i=1}^m \ln r_i = -\langle p_{Ti} \rangle \ln \prod_{i=1}^m r_i, \quad (6)$$

$$p_T = -\langle p_{Ti} \rangle_1 \sum_{i=1}^{m_1} \ln r_{1i} = -\langle p_{Ti} \rangle_1 \ln \prod_{i=1}^{m_1} r_{1i} \quad (7)$$

for the first component in the low- $p_T$  region, or

$$p_T = -\langle p_{Ti} \rangle_2 \sum_{i=1}^{m_2} \ln r_{2i} = -\langle p_{Ti} \rangle_2 \ln \prod_{i=1}^{m_2} r_{2i} \quad (8)$$

for the second component in the high- $p_T$  region,

$$y = \sigma_y \sqrt{-2 \ln R_1} \cos(2\pi R_2) + y_C, \quad (9)$$

and

$$y = \sigma_{yB} \sqrt{-2 \ln R_3} \cos(2\pi R_4) + y_B \quad (10)$$

for the first component in the backward rapidity region, or

$$y = \sigma_{yF} \sqrt{-2 \ln R_5} \cos(2\pi R_6) + y_F \quad (11)$$

for the second component in the forward rapidity region, respectively.

It should be clarified that the random numbers used above are independent in  $[0,1]$ . Through the conversions Eqs. (7), (8), (10), and (11), we can obtain a series of new values which are no longer independent in  $[0,1]$ , and obey statistically Eqs. (3) and (5) respectively. In the Monte Carlo method, Eqs. (6)–(8) are accustomed expressions which result from the Erlang distribution, and Eqs. (9)–(11) are accustomed expressions which result from the Gaussian distribution. If we use  $y = \sigma_y \sqrt{-2 \ln R_1}$  instead of Eq. (9), we obtain an accustomed expression which result from the Rayleigh distribution  $f(y) = (y/\sigma_y^2) \exp(-y^2/2\sigma_y^2)$  which is different from the Gaussian function.

The energy  $E$  is given by

$$E = \sqrt{p_T^2 + m_0^2} \cosh y, \quad (12)$$

where  $m_0$  denotes the rest mass of the considered particle. The  $x$ -,  $y$ -, and  $z$ -components of momentum  $p$  are given by

$$p_x = p_T \cos \varphi, \quad p_y = p_T \sin \varphi, \quad p_z = \sqrt{p_T^2 + m_0^2} \sinh y \quad (13)$$

respectively, where  $\varphi = 2\pi R_7$  is the azimuthal angle to distribute evenly in  $[0, 2\pi]$ . Combining with Eqs. (12) and (13), we have the velocity

$$\beta = \frac{p}{E} = \frac{\sqrt{p_T^2 + p_z^2}}{E} = \frac{\sqrt{p_x^2 + p_y^2 + p_z^2}}{E} \quad (14)$$

and its components

$$\beta_x = \frac{p_x}{E}, \quad \beta_y = \frac{p_y}{E}, \quad \beta_z = \frac{p_z}{E} \quad (15)$$

respectively. All velocity and its components are in the units of  $c$  which is the speed of light in vacuum and equals to 1 in natural units.

*Thirdly*, we describe the fitting and structuring method step by step. i) We fit the  $p_T$  and  $y$  spectra by using Eqs. (3) and (5) respectively. In the fit, the method of least square method is used to determine the values of parameters. The minimum  $\chi^2$  per degree freedom ( $\chi^2/\text{dof}$ ) corresponds to the best values of parameters. Appropriate increases or decreases in parameters determine the uncertainties on parameters, where an appropriate large  $\chi^2/\text{dof}$  is used as a limitation. Because there are correlations among parameters accounted for, we have to adjust the parameters and their uncertainties again and again. The best way is to use a multi-circulation in the calculation by the computer. ii) Using the best values of parameters, the discrete values of  $p_T$  and  $y$  are obtained by Eqs. (7) and (8), as well as (10) and (11), respectively. The discrete values of momentum and velocity components are obtained by Eqs. (13) and (15), respectively. iii) Repeating step ii) many times, we can obtain a series of discrete values. Then, particle scatter plots, i.e. event patterns, can be structured by graphic softwares.

### 3 Results and discussion

Figure 1 presents (a)(b) transverse momentum spectra,  $d^2\sigma/(dydp_T)$ , and (c)(d) rapidity spectra,  $d\sigma/dy$ , of  $Z$  bosons produced in  $pp$  collisions at  $\sqrt{s} = 2.76$  TeV for the (a)(c) dimuon ( $\mu\mu$ ) and (b)(d) dielectron ( $ee$ ) decay channels in  $|y| < 2.0$  and  $|y| < 1.44$  respectively, where  $\sigma$  on the vertical axis denotes the cross-section, and the integral luminosity  $L_{\text{int}} = 5.4 \text{ pb}^{-1}$ . The closed squares represent the experimental data of the CMS Collaboration [27], and the error bars are only the statistical uncertainties. The curves are our results calculated by using the two-component Erlang distribution for  $p_T$  spectrum and the two-component Gaussian distribution for  $y$  spectrum, which are the results of the multisource thermal model [15–17] and the revised Landau hydrodynamic model [18–26], respectively. The values of free parameters [ $m_1, \langle p_{Ti} \rangle_1, k_1, m_2, \langle p_{Ti} \rangle_2, y_F (= -y_B)$  and  $\sigma_{yF} (= \sigma_{yB})$ ], normalization constants ( $N_{p_T}$  and  $N_y$ ), and  $\chi^2/\text{dof}$  are listed in Tables 1 and 2, where the normalization constant  $N_{p_T}$  (or  $N_y$ ) is used to give comparison between the normalized curve with experimental  $p_T$  (or  $y$ ) spectrum. One can see that the results calculated by using the hybrid model are in agreement with the experimental data of  $Z$  bosons produced in  $pp$  collisions at  $\sqrt{s} = 2.76$  TeV measured by the CMS Collaboration. In some cases, the values of  $\chi^2$  are very large due to very small experimental errors.

Figure 2 is similar to Figure 1, but it shows the results in Pb-Pb collisions with 0–100% centrality at  $\sqrt{s_{NN}} = 2.76$  TeV, where the per-event yield  $N$  on the vertical axis is

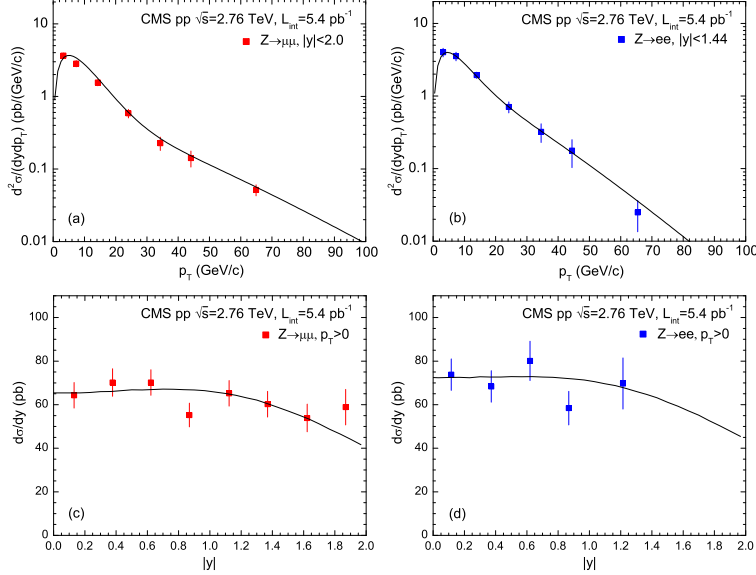


Fig. 1. (a)(b) Transverse momentum spectra and (c)(d) rapidity spectra of  $Z$  bosons produced in  $pp$  collisions at  $\sqrt{s} = 2.76$  TeV, for the (a)(c) dimuon ( $\mu\mu$ ) and (b)(d) dielectron ( $ee$ ) decay channels in  $|y| < 2.0$  and  $|y| < 1.44$  respectively, where  $\sigma$  on the vertical axis denotes the cross-section, and the integral luminosity  $L_{\text{int}} = 5.4 \text{ pb}^{-1}$ . The closed squares represent the experimental data of the CMS Collaboration [27], and the error bars are only the statistical uncertainties. The curves are our results calculated by using the (a)(b) two-component Erlang distribution and (c)(d) two-component Gaussian distribution, respectively.

used instead of the cross-section  $\sigma$ , and  $L_{\text{int}} = 150 \mu\text{b}^{-1}$ . The values of free parameters, normalization constants, and  $\chi^2/\text{dof}$  are listed in Tables 1 and 2. One can see that the results calculated by using the hybrid model are in agreement with the experimental data of  $Z$  bosons produced in Pb-Pb collisions at  $\sqrt{s_{NN}} = 2.76$  TeV measured by the CMS Collaboration. It should be noted that the ATLAS collaboration has also published similar experimental results [28, 29]. We can do similar fits for the spectra of  $p_T$  and  $y$ , which are not presented in the present work by design due to the similarity.

Table 1. Values of free parameters ( $m_1$ ,  $\langle p_{Ti} \rangle_1$ ,  $k_1$ ,  $m_2$ , and  $\langle p_{Ti} \rangle_2$ ), normalization constant ( $N_{p_T}$ ), and  $\chi^2/\text{dof}$  corresponding to the two-component Erlang distribution in Figures 1(a), 1(b), 2(a), 2(b), 5(a), 5(b), 8(a), 11(a) and 11(c), where both the uncertainties on  $m_1$  and  $m_2$  are 0 which are not listed in the columns. In some cases, dof is less than 1.

Figure	Type	$m_1$	$\langle p_{Ti} \rangle_1$ (GeV/c)	$k_1$	$m_2$	$\langle p_{Ti} \rangle_2$ (GeV/c)	$N_{p_T}$	$\chi^2/\text{dof}$
Figure 1(a)	$pp, Z \rightarrow \mu\mu$	2	$4.85 \pm 0.20$	$0.78 \pm 0.02$	2	$15.80 \pm 0.79$	$55.00 \pm 2.75$	$22.945/1$
Figure 1(b)	$pp, Z \rightarrow ee$	2	$4.10 \pm 0.20$	$0.60 \pm 0.02$	2	$11.00 \pm 0.55$	$63.00 \pm 3.15$	$7.495/1$
Figure 2(a)	Pb-Pb, $Z \rightarrow \mu\mu$	2	$3.35 \pm 0.17$	$0.45 \pm 0.02$	2	$10.60 \pm 0.53$	$(3.57 \pm 0.18) \times 10^{-7}$	$10.850/1$
Figure 2(b)	Pb-Pb, $Z \rightarrow ee$	2	$3.05 \pm 0.15$	$0.54 \pm 0.02$	2	$10.70 \pm 0.53$	$(3.85 \pm 0.19) \times 10^{-7}$	$2.606/1$
Figure 5(a)	$pp, J/\psi$	2	$1.15 \pm 0.06$	$0.95 \pm 0.02$	2	$2.34 \pm 0.12$	$5.00 \pm 0.25$	$41.272/28$
Figure 5(b)	$pp, \psi(2S)$	2	$1.30 \pm 0.07$	$0.90 \pm 0.02$	2	$2.50 \pm 0.13$	$0.75 \pm 0.04$	$2.587/15$
Figure 8(a)	$pp, \Upsilon(1S)$	2	$2.30 \pm 0.12$	$0.65 \pm 0.02$	3	$1.75 \pm 0.09$	$2.38 \pm 0.12$	$1.997/9$
	$pp, \Upsilon(2S)$	3	$1.78 \pm 0.09$	$0.68 \pm 0.02$	2	$2.80 \pm 0.14$	$0.56 \pm 0.03$	$0.506/6$
	$pp, \Upsilon(3S)$	3	$2.00 \pm 0.10$	$0.40 \pm 0.02$	2	$3.20 \pm 0.16$	$0.29 \pm 0.01$	$5.800/5$
Figure 11(a)	Pb-Pb, $J/\psi$ , 0–20%	2	$0.89 \pm 0.04$	$0.50 \pm 0.02$	3	$0.69 \pm 0.03$	$(2.50 \pm 0.13) \times 10^{-2}$	$12.872/7$
	Pb-Pb, $J/\psi$ , 20–40%	2	$0.90 \pm 0.05$	$0.40 \pm 0.02$	3	$0.78 \pm 0.04$	$(9.00 \pm 0.45) \times 10^{-3}$	$18.291/7$
	Pb-Pb, $J/\psi$ , 40–90%	2	$0.93 \pm 0.05$	$0.40 \pm 0.02$	3	$0.78 \pm 0.04$	$(1.60 \pm 0.08) \times 10^{-3}$	$29.495/7$
Figure 11(c)	Pb-Pb, $\Upsilon(1S)$	3	$1.50 \pm 0.08$	$0.35 \pm 0.02$	2	$3.00 \pm 0.15$	$0.30 \pm 0.02$	$11.024/-1$
	Pb-Pb, $\Upsilon(2S)$	3	$1.50 \pm 0.08$	$0.25 \pm 0.02$	2	$4.00 \pm 0.20$	$(1.50 \pm 0.08) \times 10^{-2}$	$0.287/-3$

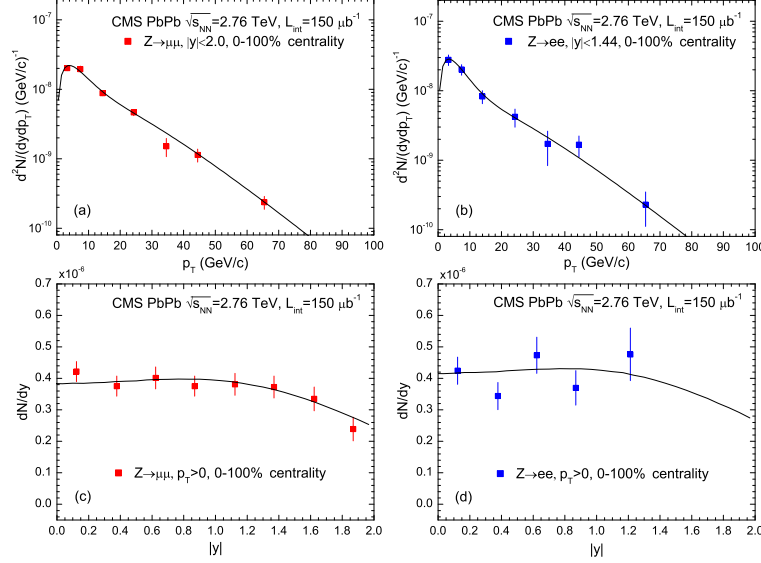


Fig. 2. Same as Figure 1, but showing the results in Pb-Pb collisions with 0–100% centrality at  $\sqrt{s_{NN}} = 2.76$  TeV, where the per-event yield  $N$  on the vertical axis is used instead of the cross-section  $\sigma$ , and  $L_{int} = 150 \mu\text{b}^{-1}$ .

Table 2. Values of free parameter [ $y_F$  ( $= -y_B$ ) and  $\sigma_{yF}$  ( $= \sigma_{yB}$ )], normalization constant ( $N_y$ ), and  $\chi^2/\text{dof}$  corresponding to the two-component Gaussian distribution in Figures 1(c), 1(d), 2(c), 2(d), 5(c), 5(d), 8(b), 8(c), 8(d), 11(b), and 11(d). In some cases, dof is less than 1.

Figure	Type	$y_F$ ( $= -y_B$ )	$\sigma_{yF}$ ( $= \sigma_{yB}$ )	$N_y$	$\chi^2/\text{dof}$
Figure 1(c)	$pp, Z \rightarrow \mu\mu$	$1.10 \pm 0.03$	$1.00 \pm 0.05$	$300 \pm 15$	$8.622/5$
Figure 1(d)	$pp, Z \rightarrow ee$	$1.10 \pm 0.03$	$1.05 \pm 0.05$	$330 \pm 17$	$2.074/2$
Figure 2(c)	Pb-Pb, $Z \rightarrow \mu\mu$	$1.12 \pm 0.03$	$1.00 \pm 0.05$	$1.80 \pm 0.09$	$2.860/5$
Figure 2(d)	Pb-Pb, $Z \rightarrow ee$	$1.12 \pm 0.03$	$1.00 \pm 0.05$	$1.95 \pm 0.10$	$5.626/2$
Figure 5(c)	$pp, J/\psi$	$1.90 \pm 0.03$	$1.82 \pm 0.09$	$54 \pm 3$	$8.141/14$
Figure 5(d)	$pp, \psi(2S)$	$1.90 \pm 0.03$	$1.85 \pm 0.10$	$8.8 \pm 0.4$	$1.338/3$
Figure 8(b)	$pp, \Upsilon(1S)$	$1.58 \pm 0.03$	$1.65 \pm 0.08$	$13.00 \pm 0.65$	$0.492/2$
	$pp, \Upsilon(2S)$	$1.55 \pm 0.03$	$1.48 \pm 0.07$	$3.20 \pm 0.16$	$0.657/2$
	$pp, \Upsilon(3S)$	$1.55 \pm 0.03$	$1.60 \pm 0.08$	$1.50 \pm 0.08$	$0.395/2$
Figure 8(c)	$pp, \Upsilon(1S)$	$1.58 \pm 0.03$	$1.65 \pm 0.08$	$510 \pm 26$	$22.156/17$
Figure 8(d)	$pp, \Upsilon(2S)$	$1.55 \pm 0.03$	$1.48 \pm 0.07$	$160 \pm 8$	$5.760/9$
Figure 11(b)	Pb-Pb, $J/\psi$ , inclusive	$1.40 \pm 0.03$	$1.70 \pm 0.09$	$17.00 \pm 0.85$	$0.504/0$
	Pb-Pb, $J/\psi$ , prompt	$1.51 \pm 0.03$	$1.70 \pm 0.09$	$13.70 \pm 0.69$	$0.899/0$
Figure 11(d)	Pb-Pb, $\Upsilon(1S)$	$1.35 \pm 0.03$	$1.25 \pm 0.06$	$1.95 \pm 0.10$	$1.070/3$
	Pb-Pb, $\Upsilon(2S)$	$1.38 \pm 0.03$	$1.22 \pm 0.06$	$0.16 \pm 0.008$	$0.085/-1$

Based on the parameter values obtained from Figures 1 and 2, we can perform a Monte Carlo calculation and obtain a series of kinematic quantities. For example, event patterns in two-dimensional  $p_T - y$  space are presented in Figure 3 for (a)(c)  $Z \rightarrow \mu\mu$  and (b)(d)  $Z \rightarrow ee$  channels in (a)(b)  $pp$  collisions at  $\sqrt{s} = 2.76$  TeV and (c)(d) Pb-Pb collisions at  $\sqrt{s_{NN}} = 2.76$  TeV. The total number of particles for each panel is 1000. The squares and circles represent the contributions of the first and second components in the two-component Erlang distribution for  $p_T$  spectrum respectively. Most particles appear in the region of low- $p_T$  and low- $|y|$ . The values of root-mean-squares ( $\sqrt{p_T^2}$  for  $p_T$  and  $\sqrt{y^2}$  for  $y$ ) are listed in Table 3. In the calculation, the contributions of the first and

second components in the two-component Gaussian distribution for  $y$  spectrum are not distinguished by design.

Figure 4 is another example of event pattern in three-dimensional velocity ( $\beta_x - \beta_y - \beta_z$ ) space for (a)(c)  $Z \rightarrow \mu\mu$  and (b)(d)  $Z \rightarrow ee$  channels in (a)(b)  $pp$  collisions at  $\sqrt{s} = 2.76$  TeV and (c)(d) Pb-Pb collisions at  $\sqrt{s_{NN}} = 2.76$  TeV. The total number of particles for each panel is 1000. The red and blue globules represent the contributions of the first and second components in the two-component Erlang distribution for  $p_T$  spectrum respectively. Most particles appear in the region of low- $|\beta_x|$  and low- $|\beta_y|$ . The values of root-mean-squares ( $\sqrt{\beta_x^2}$  for  $\beta_x$ ,  $\sqrt{\beta_y^2}$  for  $\beta_y$ , and  $\sqrt{\beta_z^2}$  for  $\beta_z$ ) and the maximum  $|\beta_x|$ ,  $|\beta_y|$ , and  $|\beta_z|$  ( $|\beta_x|_{\max}$ ,  $|\beta_y|_{\max}$ , and  $|\beta_z|_{\max}$ ) are listed in Table 4. One can see that  $\sqrt{\beta_x^2} \approx \sqrt{\beta_y^2} \ll \sqrt{\beta_z^2}$ , and  $|\beta_x|_{\max} \approx |\beta_y|_{\max} < |\beta_z|_{\max}$ . The event pattern in velocity (or coordinate) space looks like a rough cylinder along  $oz$  axis (the beam direction) when it emit  $Z$  bosons, and the maximum velocity surface (the surface consisted of the maximum velocities in different directions) is a fat cylinder which has the length being 1.6–2.2 times of diameter. As for Figure 3, the contributions of the first and second components in the two-component Gaussian distribution for  $y$  spectrum are not distinguished by design.

In Figure 5, the spectra of inclusive (a)  $J/\psi$   $p_T$ , (b)  $\psi(2S)$   $p_T$ , (c)  $J/\psi$   $y$ , and (d)  $\psi(2S)$   $y$  mesons in  $pp$  collisions at  $\sqrt{s} = 7$  TeV are displayed. Different solid symbols represent different data measured by the ALICE [30–32] and LHCb collaborations [33, 34] in different conditions shown in the panels, and the error bars are only the statistical uncertainties. The curves for  $p_T$  and  $y$  spectra are our results calculated by using the two-component Erlang distribution for  $p_T$  spectrum and the two-component Gaussian distribution for  $y$  spectrum respectively. The values of free parameters, normalization constants, and  $\chi^2/\text{dof}$  are listed in Tables 1 and 2. One can see that the results calculated by using the hybrid model are in agreement with the experimental data of quarkonium states (charmonium  $c\bar{c}$  mesons  $J/\psi$  and  $\psi(2S)$ ) produced in  $pp$  collisions at  $\sqrt{s} = 7$  TeV measured by the ALICE and LHCb Collaborations.

Based on the parameter values obtained from Figure 5, we can obtain some event patterns for  $J/\psi$  and  $\psi(2S)$ . In Figures 6 and 7, the event patterns in  $p_T - y$  and  $\beta_x - \beta_y - \beta_z$  spaces for (a) inclusive  $J/\psi$  mesons and (b) inclusive  $\psi(2S)$  mesons are given. The red squares and globules represent the contribution of the first component, and the blue circles and globules represent the contribution of the second component, in the two-component Erlang distribution for  $p_T$  spectrum. The corresponding values of root-mean squares and the maximum velocity components are listed in Tables 3 and 4. One can see that  $\sqrt{p_T^2}$  ( $\sqrt{y^2}$ ) for charmonium  $c\bar{c}$  mesons is less (greater) than that for  $Z$  bosons. Once again,  $\sqrt{\beta_x^2} \approx \sqrt{\beta_y^2} \ll \sqrt{\beta_z^2}$ , and  $|\beta_x|_{\max} \approx |\beta_y|_{\max} < |\beta_z|_{\max}$ . At the same time,  $\sqrt{\beta_x^2}$  and  $|\beta_x|_{\max}$  ( $\sqrt{\beta_y^2}$  and  $|\beta_y|_{\max}$ ,  $\sqrt{\beta_z^2}$ ) for charmonium  $c\bar{c}$  mesons are larger than those for  $Z$  bosons, and the two types of particles have nearly the same  $|\beta_z|_{\max}$ . The event pattern in velocity (or coordinate) space looks like a rough cylinder along the beam direction when it emit charmonium  $c\bar{c}$  mesons, and the maximum velocity surface is a fat cylinder which has the length being 1.2–1.4 times of diameter.



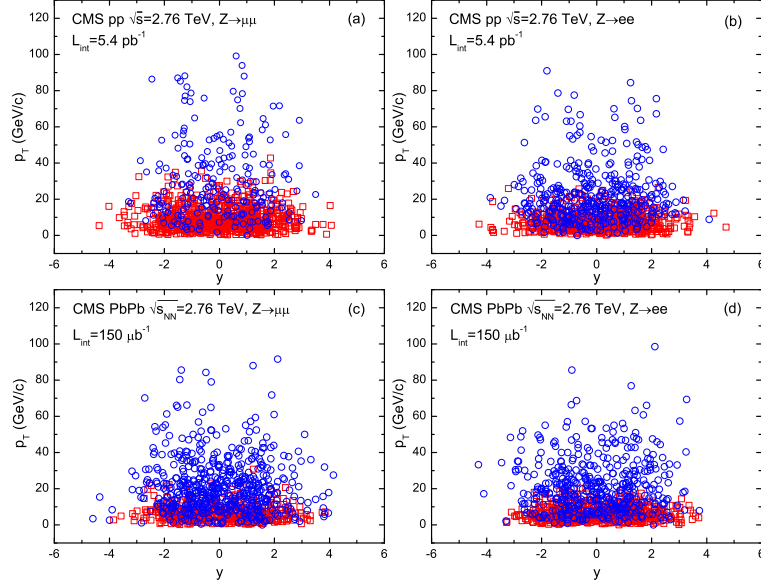


Fig. 3. Event patterns (particle scatter plots) in two-dimensional  $p_T - y$  space in (a)(b)  $pp$  collisions at  $\sqrt{s} = 2.76$  TeV and (c)(d) Pb-Pb collisions at  $\sqrt{s_{NN}} = 2.76$  TeV, for the (a)(c) dimuon and (b)(d) dielectron decay channels. The number of  $Z$  bosons for each panel is 1000. The squares and circles represent the results of the first and second components in the two-component Erlang distribution for  $p_T$ , respectively. The contributions of the first and second components in the two-component Gaussian distribution for  $y$  are not distinguished by design.

Table 3. Values of the root-mean-squares  $\sqrt{p_T^2}$  for  $p_T$  and  $\sqrt{y^2}$  for  $y$  corresponding to the particle scatter plots in Figures 3, 6, 9, and 12.

Figure	Type	$\sqrt{p_T^2}$ (GeV/c)	$\sqrt{y^2}$
Figure 3(a)	$pp, Z \rightarrow \mu\mu$	$18.91 \pm 0.72$	$1.50 \pm 0.03$
Figure 3(b)	$pp, Z \rightarrow ee$	$19.05 \pm 0.69$	$1.49 \pm 0.03$
Figure 3(c)	Pb-Pb, $Z \rightarrow \mu\mu$	$20.38 \pm 0.66$	$1.50 \pm 0.03$
Figure 3(d)	Pb-Pb, $Z \rightarrow ee$	$18.82 \pm 0.64$	$1.47 \pm 0.03$
Figure 6(a)	$pp, J/\psi$	$3.11 \pm 0.09$	$2.68 \pm 0.05$
Figure 6(b)	$pp, \psi(2S)$	$3.40 \pm 0.09$	$2.67 \pm 0.05$
Figure 9(a)	$pp, \Upsilon(1S)$	$5.53 \pm 0.11$	$2.26 \pm 0.05$
Figure 9(b)	$pp, \Upsilon(2S)$	$6.03 \pm 0.11$	$2.13 \pm 0.04$
Figure 9(c)	$pp, \Upsilon(3S)$	$6.49 \pm 0.11$	$2.23 \pm 0.04$
Figure 12(a)	Pb-Pb, $\Upsilon(1S)$	$6.26 \pm 0.14$	$1.88 \pm 0.04$
Figure 12(b)	Pb-Pb, $\Upsilon(2S)$	$7.80 \pm 0.15$	$1.83 \pm 0.03$

In the upper panel of Figure 8, the spectra of (a)  $p_T$  for  $\Upsilon(1S)$ ,  $\Upsilon(2S)$ , and  $\Upsilon(3S)$  and (b)  $y$  in backward (forward) region for  $\Upsilon(1S)$ ,  $\Upsilon(2S)$ , and  $\Upsilon(3S)$  produced in  $pp$  collisions at  $\sqrt{s} = 7$  TeV are presented, where  $\sigma^{iS}$  and  $B^{iS}$  on the vertical axis denote the cross-section and branching fractions of  $\Upsilon(iS)$  ( $i = 1, 2$ , and  $3$ ), respectively. The closed circles, squares, and triangles represent the experimental data of  $\Upsilon(1S)$ ,  $\Upsilon(2S)$ , and  $\Upsilon(3S)$ , respectively, measured by the LHCb Collaboration [35], and the error bars are the total uncertainties which combine the systematic and statistical uncertainties to be equal to their root-sum-square. The curves for  $p_T$  and  $y$  spectra are our results calculated by using the two-component Erlang distribution and the two-component Gaussian distribution

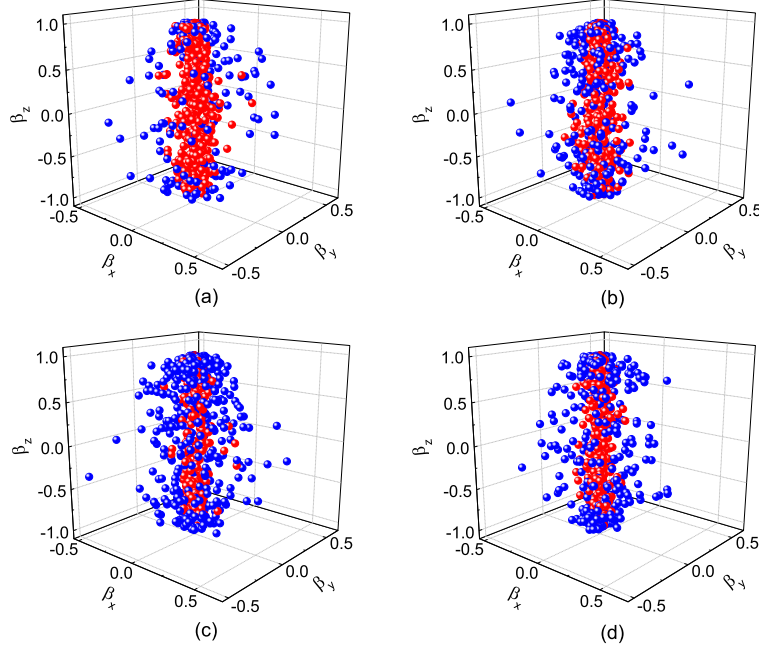


Fig. 4. Event patterns in three-dimensional velocity ( $\beta_x - \beta_y - \beta_z$ ) space in (a)(b)  $pp$  collisions at  $\sqrt{s} = 2.76$  TeV and (c)(d) Pb-Pb collisions at  $\sqrt{s_{NN}} = 2.76$  TeV, for the (a)(c) dimuon and (b)(d) dielectron decay channels. The number of  $Z$  bosons for each panel is 1000. The red and blue globules represent the results of the first and second components in the two-component Erlang distribution for  $p_T$ , respectively. The contributions of the first and second components in the two-component Gaussian distribution for  $y$  are not distinguished by design.

respectively. The values of free parameters, normalization constants, and  $\chi^2/\text{dof}$  are listed in Tables 1 and 2. One can see that the results calculated by using the hybrid model are in agreement with the experimental data of quarkonium states (bottomonium  $b\bar{b}$  mesons  $\Upsilon(1S)$ ,  $\Upsilon(2S)$ , and  $\Upsilon(3S)$ ) measured by the LHCb Collaboration.

Table 4. Values of the root-mean-squares  $\sqrt{\beta_x^2}$  for  $\beta_x$ ,  $\sqrt{\beta_y^2}$  for  $\beta_y$ , and  $\sqrt{\beta_z^2}$  for  $\beta_z$ , as well as the maximum  $|\beta_x|$ ,  $|\beta_y|$ , and  $|\beta_z|$  ( $|\beta_x|_{\text{max}}$ ,  $|\beta_y|_{\text{max}}$ , and  $|\beta_z|_{\text{max}}$ ) corresponding to the particle scatter plots in Figures 4, 7, 10, and 13.

Figure	Type	$\sqrt{\beta_x^2}$ (c)	$\sqrt{\beta_y^2}$ (c)	$\sqrt{\beta_z^2}$ (c)	$ \beta_x _{\text{max}}$ (c)	$ \beta_y _{\text{max}}$ (c)	$ \beta_z _{\text{max}}$ (c)
Figure 4(a)	$pp, Z \rightarrow \mu\mu$	$0.08 \pm 0.01$	$0.09 \pm 0.01$	$0.76 \pm 0.01$	0.56	0.47	1.00
Figure 4(b)	$pp, Z \rightarrow ee$	$0.09 \pm 0.01$	$0.08 \pm 0.01$	$0.76 \pm 0.01$	0.56	0.60	1.00
Figure 4(c)	Pb-Pb, $Z \rightarrow \mu\mu$	$0.09 \pm 0.01$	$0.10 \pm 0.01$	$0.75 \pm 0.01$	0.65	0.54	1.00
Figure 4(d)	Pb-Pb, $Z \rightarrow ee$	$0.08 \pm 0.01$	$0.08 \pm 0.01$	$0.76 \pm 0.01$	0.54	0.45	1.00
Figure 7(a)	$pp, J/\psi$	$0.16 \pm 0.01$	$0.17 \pm 0.01$	$0.90 \pm 0.01$	0.83	0.76	1.00
Figure 7(b)	$pp, \psi(2S)$	$0.20 \pm 0.01$	$0.21 \pm 0.01$	$0.88 \pm 0.01$	0.84	0.77	1.00
Figure 10(a)	$pp, \Upsilon(1S)$	$0.14 \pm 0.01$	$0.14 \pm 0.01$	$0.85 \pm 0.01$	0.79	0.61	1.00
Figure 10(b)	$pp, \Upsilon(2S)$	$0.13 \pm 0.01$	$0.13 \pm 0.01$	$0.83 \pm 0.01$	0.67	0.67	1.00
Figure 10(c)	$pp, \Upsilon(3S)$	$0.19 \pm 0.01$	$0.19 \pm 0.01$	$0.84 \pm 0.01$	0.74	0.76	1.00
Figure 13(a)	Pb-Pb, $\Upsilon(1S)$	$0.19 \pm 0.01$	$0.17 \pm 0.01$	$0.81 \pm 0.01$	0.81	0.78	1.00
Figure 13(b)	Pb-Pb, $\Upsilon(2S)$	$0.21 \pm 0.01$	$0.22 \pm 0.01$	$0.81 \pm 0.01$	0.79	0.83	1.00

To study further the  $y$  spectra of bottomonium  $b\bar{b}$  mesons, Figures 8(c) and 8(d) give the results for  $\Upsilon(1S)$  and  $\Upsilon(2S)$  in  $pp$  collisions at 7 TeV respectively. Different closed

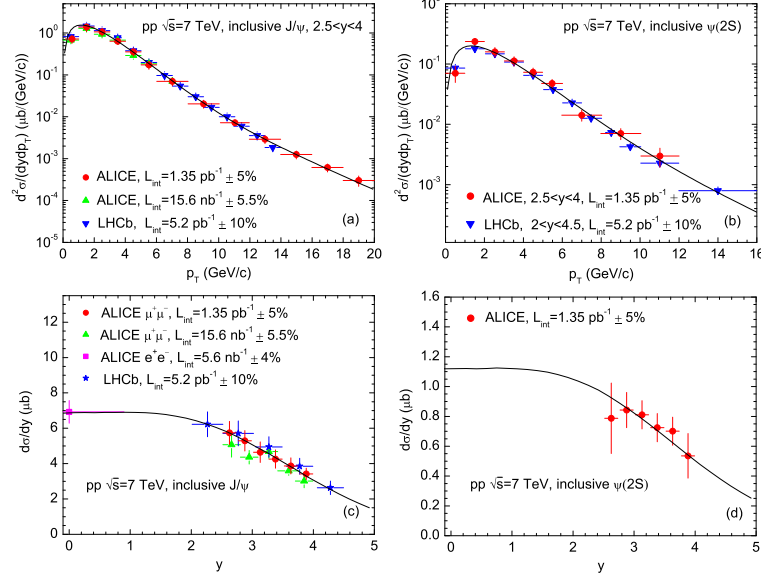


Fig. 5. (a)(b) Transverse momentum spectra and (c)(d) rapidity spectra of (a)(c) inclusive  $J/\psi$  mesons and (b)(d) inclusive  $\psi(2S)$  mesons produced in  $pp$  collisions at  $\sqrt{s} = 7$  TeV. The closed symbols represent the experimental data of the ALICE [30–32] and LHCb Collaboration [33, 34] in different conditions shown in the panels, and the error bars are only the statistical uncertainties. The curves are our results calculated by using the hybrid model.

symbols represent different data measured by the ALICE [30], LHCb [35], and CMS collaborations [36, 37] in different conditions shown in the panels, and the error bars are only the systematic uncertainties. The curves are our results calculated by using the two-component Gaussian distribution. The values of free parameters, normalization constants, and  $\chi^2/\text{dof}$  are listed in Table 2. One can see that the results calculated by using the revised Landau hydrodynamic model are in indeed agreement with the experimental data of bottomonium  $b\bar{b}$  mesons  $\Upsilon(1S)$  and  $\Upsilon(2S)$ .

Based on the parameter values obtained from Figures 8(a) and 8(b), we can obtain some event patterns for  $\Upsilon(1S)$ ,  $\Upsilon(2S)$ , and  $\Upsilon(3S)$ . In Figures 9 and 10, the event patterns in  $p_T - y$  and  $\beta_x - \beta_y - \beta_z$  spaces for (a)  $\Upsilon(1S)$ , (b)  $\Upsilon(2S)$ , and (c)  $\Upsilon(3S)$  are given. The red squares and globules represent the contribution of the first component, and the blue circles and globules represent the contribution of the second component, in the two-component Erlang distribution. The corresponding values of root-mean squares and the maximum velocity components are listed in Tables 3 and 4. One can see that  $\sqrt{p_T^2}$  ( $\sqrt{y^2}$ ) for bottomonium  $b\bar{b}$  mesons is close to that for charmonium  $c\bar{c}$  mesons, and less (greater) than that for  $Z$  bosons. Once more,  $\sqrt{\beta_x^2} \approx \sqrt{\beta_y^2} \ll \sqrt{\beta_z^2}$ , and  $|\beta_x|_{\text{max}} \approx |\beta_y|_{\text{max}} < |\beta_z|_{\text{max}}$ . At the same time,  $\sqrt{\beta_x^2}$  and  $|\beta_x|_{\text{max}}$  ( $\sqrt{\beta_y^2}$  and  $|\beta_y|_{\text{max}}$ ,  $\sqrt{\beta_z^2}$ ) for bottomonium  $b\bar{b}$  mesons are close to those for charmonium  $c\bar{c}$  mesons, and larger than those for  $Z$  bosons. The three types of particles have nearly the same  $|\beta_z|_{\text{max}}$ . The event pattern in velocity (or coordinate) space looks like a rough cylinder along the beam direction when it emit

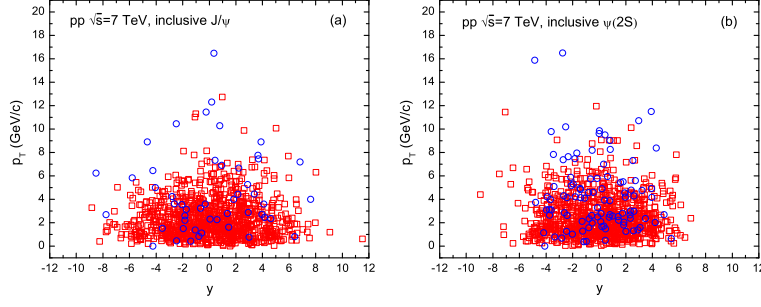


Fig. 6. Same as Figure 3, but showing the results for (a) inclusive  $J/\psi$  mesons and (b) inclusive  $\psi(2S)$  mesons produced in  $pp$  collisions at  $\sqrt{s} = 7$  TeV.

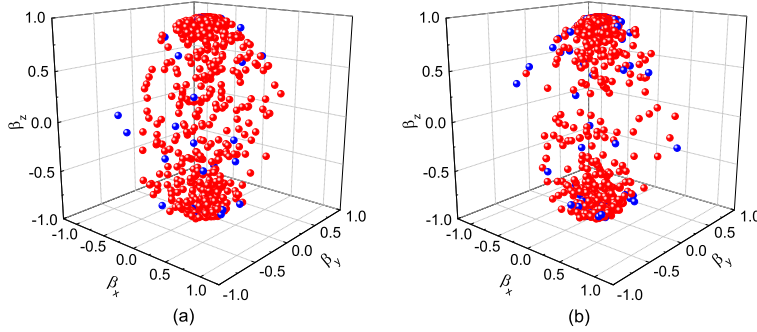


Fig. 7. Same as Figure 4, but showing the results for (a) inclusive  $J/\psi$  mesons and (b) inclusive  $\psi(2S)$  mesons produced in  $pp$  collisions at  $\sqrt{s} = 7$  TeV.

bottomonium  $b\bar{b}$  mesons, and the maximum velocity surface is a fat cylinder which has the length being 1.3–1.6 times of diameter.

The distributions of inclusive  $J/\psi$   $p_T$ , inclusive and prompt  $J/\psi$   $y$ ,  $\Upsilon(1S)$  and  $\Upsilon(2S)$   $p_T$ , as well as  $\Upsilon(1S)$  and  $\Upsilon(2S)$   $y$  in Pb-Pb collisions at  $\sqrt{s_{NN}} = 2.76$  TeV are presented in Figures 11(a)–11(d), respectively, where  $Y$  on the vertical axis denotes the yield, and  $T_{AA}$  denotes the nuclear overlap function which depends on the collision centrality. The closed symbols represent the experimental data of the ALICE [38] and CMS Collaborations [39, 40] measured in different conditions shown in the panels, and the error bars are only the systematic uncertainties. The curves are our results calculated by using the hybrid model in which the  $p_T$  and  $y$  spectra are described by the two-component Erlang distribution and the two-component Gaussian distribution respectively. The values of free parameters, normalization constants, and  $\chi^2/\text{dof}$  are listed in Tables 1 and 2. One can see that the results calculated by using the hybrid model are in agreement with the experimental data of quarkonium states ( $J/\psi$ ,  $\Upsilon(1S)$ , and  $\Upsilon(2S)$ ) measured by the ALICE and CMS Collaborations.

Because Figures 11(a) and 11(b) are the data set from different experimental conditions, we do not extract the event patterns from them. Based on the parameter values obtained from Figures 11(c) and 11(d), we obtain some event patterns for (a)  $\Upsilon(1S)$  and (b)  $\Upsilon(2S)$  in Figures 12 and 13, where the event patterns in  $p_T - y$  and  $\beta_x - \beta_y - \beta_z$  spaces are given respectively. The red squares and globules represent the contribution of

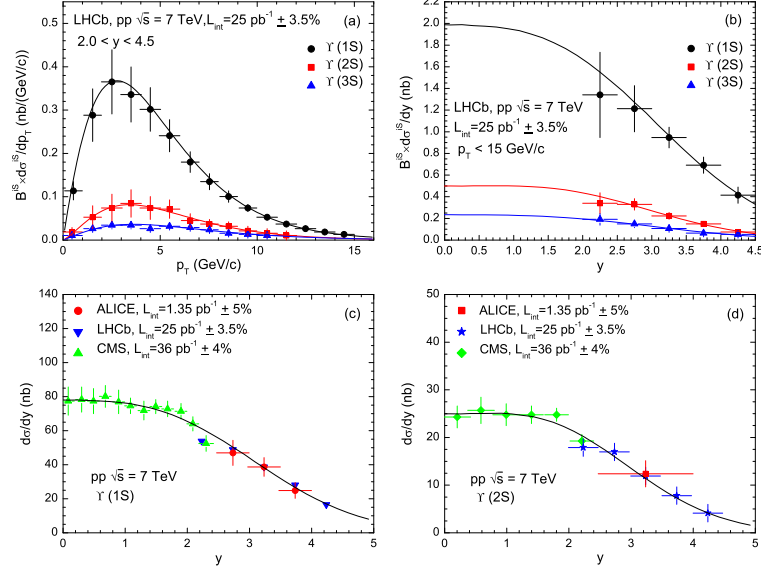


Fig. 8. (a) Transverse momentum spectra and (b) backward (forward) region rapidity spectra of bottomonium  $b\bar{b}$  mesons  $\Upsilon(1S)$ ,  $\Upsilon(2S)$ , and  $\Upsilon(3S)$ , as well as whole space rapidity spectra of (c)  $\Upsilon(1S)$  and (d)  $\Upsilon(2S)$  mesons produced in  $pp$  collisions at  $\sqrt{s} = 7$  TeV, where  $\sigma^{iS}$  and  $B^{iS}$  on the vertical axis in (a)(b) denote the cross-section and branching fractions of  $\Upsilon(iS)$  ( $i = 1, 2$ , and  $3$ ), respectively. The closed symbols represent the experimental data of the LHCb [35], ALICE [30], and CMS Collaborations [36, 37]. The error bars in (a)(b) are the total uncertainties which combine the systematic and statistical uncertainties to be equal to their root-sum-square, and the error bars in (c)(d) are only the systematic uncertainties. The curves are our results calculated by using the hybrid model.

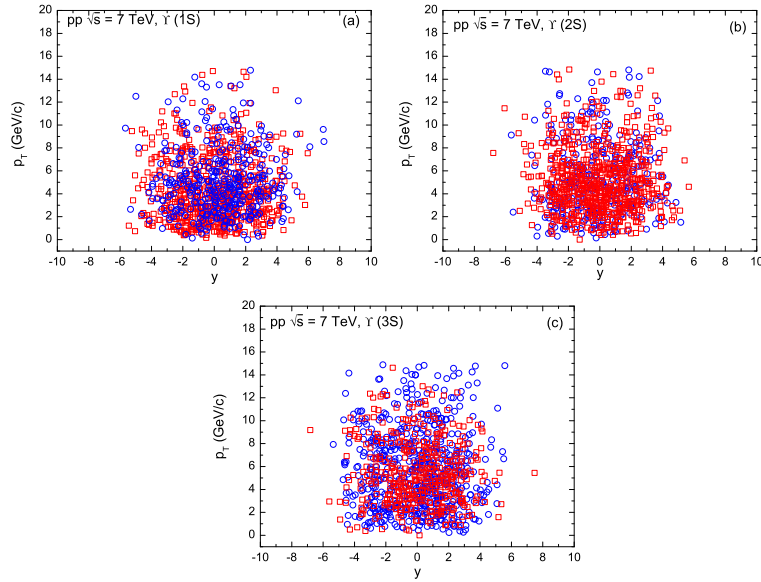


Fig. 9. Same as Figure 3, but showing the results for (a)  $\Upsilon(1S)$ , (b)  $\Upsilon(2S)$ , and (c)  $\Upsilon(3S)$  mesons produced in  $pp$  collisions at  $\sqrt{s} = 7$  TeV.

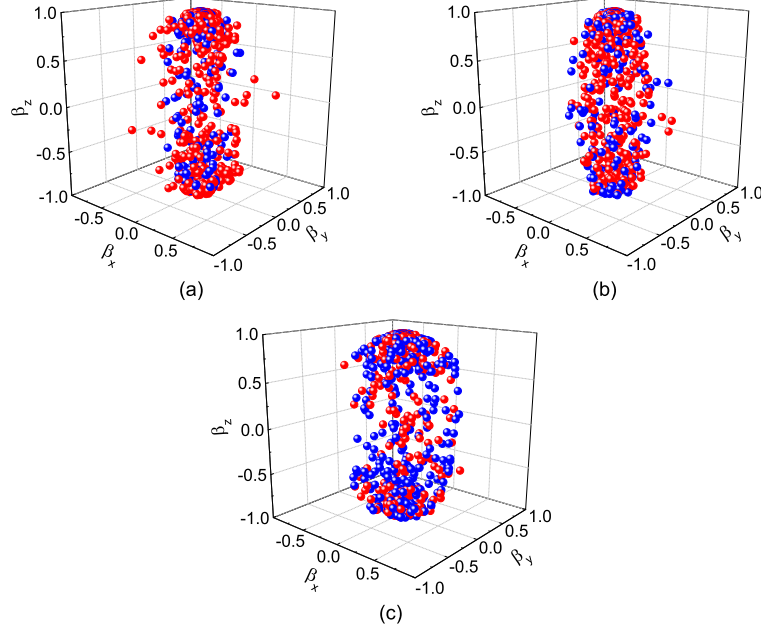


Fig. 10. Same as Figure 4, but showing the results for (a)  $\Upsilon(1S)$ , (b)  $\Upsilon(2S)$ , and (c)  $\Upsilon(3S)$  mesons produced in  $pp$  collisions at  $\sqrt{s} = 7$  TeV.

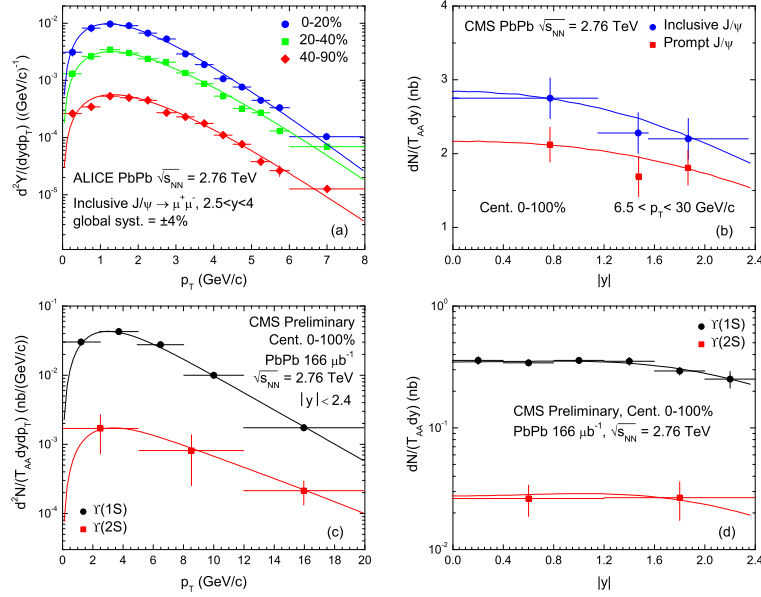


Fig. 11. (a) Transverse momentum spectra and (b) rapidity spectra of  $J/\psi$  mesons, as well as (c) transverse momentum spectra and (d) rapidity spectra of  $\Upsilon(1S)$  and  $\Upsilon(2S)$  mesons, produced in Pb-Pb collisions at  $\sqrt{s_{NN}} = 2.76$  TeV, where  $Y$  on the vertical axis denotes the yield, and  $T_{AA}$  denotes the nuclear overlap function which depends on the collision centrality. The closed symbols represent the (preliminary) experimental data of the ALICE [38] and CMS Collaborations [39, 40] in different conditions shown in the panels, and the error bars are only the systematic uncertainties. The curves are our results calculated by using the hybrid model.

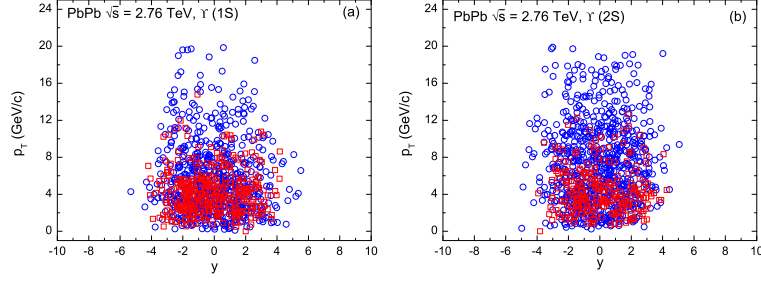


Fig. 12. Same as Figure 3, but showing the results for (a)  $\Upsilon(1S)$  and (b)  $\Upsilon(2S)$  mesons produced in Pb-Pb collisions at  $\sqrt{s} = 2.76$  TeV.

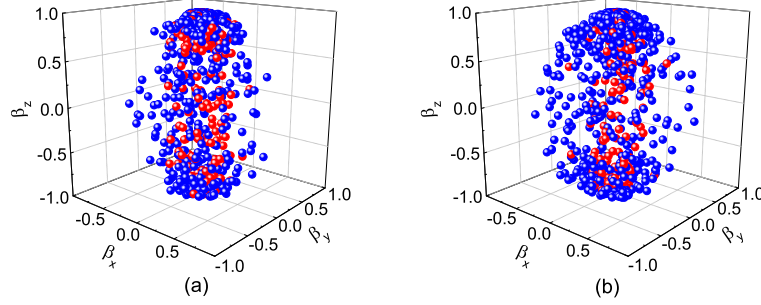


Fig. 13. Same as Figure 4, but showing the results for (a)  $\Upsilon(1S)$  and (b)  $\Upsilon(2S)$  mesons produced in Pb-Pb collisions at  $\sqrt{s} = 2.76$  TeV.

the first component, and the blue circles and globules represent the contribution of the second component, in the two-component Erlang distribution. The corresponding values of root-mean squares and the maximum velocity components are listed in Tables 3 and 4. One can see the same or similar conclusion as that from Figures 9 and 10. The maximum velocity surface is a fat cylinder which has the length being 1.2–1.3 times of diameter.

We can give qualitatively a prediction on the prospects to actually get  $J/\psi$  rapidity distributions in Figure 11(b) for the given centrality classes listed in Figure 11(a). From Table 1 we see that  $\langle p_{Ti} \rangle_1$  and  $\langle p_{Ti} \rangle_2$  for Figure 11(a) increase slightly with decrease of the centrality. As a non-leading particle, the rapidity distribution of  $J/\psi$  does not depend obviously on the centrality. These two characteristics render that in the derived event pattern, the particles will scatter slightly in higher  $p_T$  region in peripheral collisions. From central to peripheral collisions, the increase in  $p_T$  is slight due to the slight increases in  $\langle p_{Ti} \rangle_1$  and  $\langle p_{Ti} \rangle_2$ .

The most important set of parameters in Table 1 are the mean contributions,  $\langle p_{Ti} \rangle_1$  and  $\langle p_{Ti} \rangle_2$ , of each source for  $p_T$  spectrum in the first and second components. Then, the mean contribution of each source in the first+second components is  $\langle p_{Ti} \rangle = \langle p_T \rangle / [k_1 m_1 + (1 - k_1) m_2]$ . The mean transverse momenta contributed by the first and second components are  $m_1 \langle p_{Ti} \rangle_1$  and  $m_2 \langle p_{Ti} \rangle_2$  respectively. The most important set of parameters in Table 2 are the peak position  $y_F$  ( $y_B$ ) and distribution width  $\sigma_{yF}$  ( $\sigma_{yB}$ ) for the forward (backward) region in the two-component Gaussian function for  $y$  spectrum. To see the dependences of these parameters on  $m_0$ , Figure 14 shows the relations between (a)  $\langle p_{Ti} \rangle$  ( $\langle p_{Ti} \rangle_1$ ,  $\langle p_{Ti} \rangle_2$ )



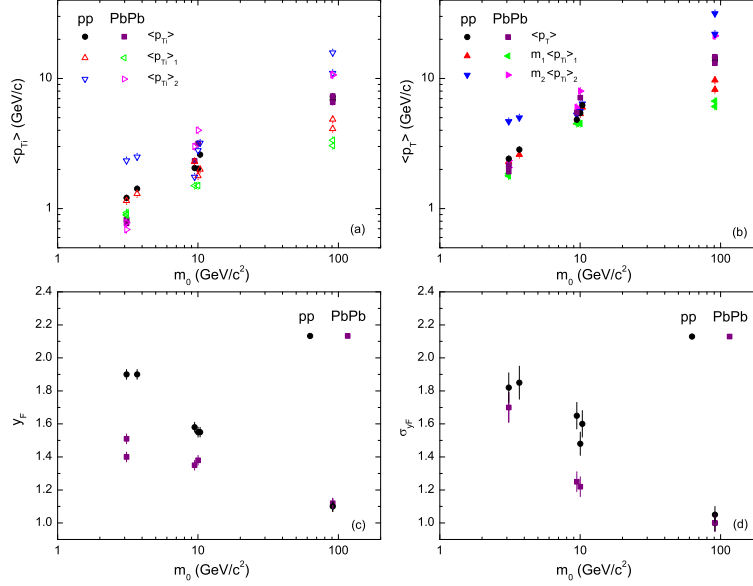


Fig. 14. Relations between (a)  $\langle p_{Ti} \rangle$  ( $\langle p_{Ti} \rangle_1$ ,  $\langle p_{Ti} \rangle_2$ ) and  $m_0$ , (b)  $\langle p_T \rangle$  ( $m_1 \langle p_{Ti} \rangle_1$ ,  $m_2 \langle p_{Ti} \rangle_2$ ) and  $m_0$ , (c)  $y_F$  and  $m_0$ , as well as (d)  $\sigma_{y_F}$  and  $m_0$ , in  $pp$  and Pb-Pb collisions. Different symbols represent different parameters for different collisions shown in the panels, where  $\langle p_{Ti} \rangle$ ,  $\langle p_{Ti} \rangle_1$ , and  $\langle p_{Ti} \rangle_2$  denote the source's mean contributions in the first+second, first, and second components, respectively; and  $\langle p_T \rangle$ ,  $m_1 \langle p_{Ti} \rangle_1$ , and  $m_2 \langle p_{Ti} \rangle_2$  denote the mean transverse momenta contributed by the first+second, first, and second components, respectively.

and  $m_0$ , (b)  $\langle p_T \rangle$  ( $m_1 \langle p_{Ti} \rangle_1$ ,  $m_2 \langle p_{Ti} \rangle_2$ ) and  $m_0$ , (c)  $y_F$  and  $m_0$ , as well as (d)  $\sigma_{y_F}$  and  $m_0$ , in  $pp$  and Pb-Pb collisions. Different symbols represent different parameters for different collisions shown in the panels. One can see an obvious increase in  $\langle p_{Ti} \rangle$ ,  $\langle p_{Ti} \rangle_1$ ,  $\langle p_{Ti} \rangle_2$ ,  $\langle p_T \rangle$ ,  $m_1 \langle p_{Ti} \rangle_1$ , and  $m_2 \langle p_{Ti} \rangle_2$ , and a decrease in  $y_F$  and  $\sigma_{y_F}$ , when  $m_0$  changes from  $\sim 3$  GeV to  $\sim 90$  GeV. This mass scale imposes a difference on the observed data from the presence of a quantum chromodynamics (QCD) hard scale.

From Table 1 one can see that in some cases  $k_1$  is less than 0.5, and  $\langle p_{Ti} \rangle_1$  is greater than  $\langle p_{Ti} \rangle_2$ . These results does not mean a reversal of the first and second components, or a reversal of the low- and high- $p_T$  regions. In fact, the first component that contributes in the low- $p_T$  region is determined by both  $m_1$  and  $\langle p_{Ti} \rangle_1$ , and the second component that contributes in the high- $p_T$  region is determined by both  $m_2$  and  $\langle p_{Ti} \rangle_2$ . The mean transverse momenta,  $m_1 \langle p_{Ti} \rangle_1$  and  $m_2 \langle p_{Ti} \rangle_2$ , contributed by the first and second components, respectively, play a determinate action. Generally, we restrict  $m_1 \langle p_{Ti} \rangle_1 < m_2 \langle p_{Ti} \rangle_2$ , which ensures the first component contributing in the low- $p_T$  region and the second component contributing in the high- $p_T$  region. The size of  $k_1$  is not related to the relative sizes of  $m_1 \langle p_{Ti} \rangle_1$  and  $m_2 \langle p_{Ti} \rangle_2$ .

We would like to point out that  $Z$  bosons and quarkonium states are chosen by us in the present work due to their productions being through hard scattering and at initial state, which are different from those of light flavor particles which are mostly produced through soft excitation and at intermediate state. Although we describe uniformly the



presence of a variable mass scale from 3 to 90 GeV, we cannot provide further information in theory. In fact, the method used in the present work is independent of models, which is only based on the description of probability distribution of experimental data. If we do not use formulas, but discrete probabilities based on data, similar event patterns can be obtained. In addition, our choices on data sets are not sole. In fact, other data sets which contained both  $p_T$  and  $y$  spectra can be used to structure the event patterns.

It should be noted that in the calculation of  $\chi^2$  in Figures 1, 2, 5, 8 and 11, we have to determine the corresponding relation between a theoretical point and an experimental data in a given bin of a variable. According to ref. [41], there are more than one methods to determine the corresponding relation, which include considerations in variable and frequency respectively. In the present work, we have simply used the method of histograms, i.e. presenting the theoretical point and experimental data in the form of histograms when we calculate  $\chi^2$ . In most cases, if the bin is narrow enough, to use the closest theoretical point and experimental data is an approximate alternative method.

It should also be noted that Figures 3, 4, 6, 7, 9, 10, 12, 13 are supposed to only give pictorial representations of the particle scatter plots at the stage of kinetic freeze-out of the interacting system. These pictorial representations are based on the experimental data themselves. They are independent of models due to Eqs. (3) and (5) being only parameterizations of the experimental data, and Eqs. (7), (8), (10), and (11) being only stochastic extractions based on Eqs. (3) and (5). Any other event generators that describe simultaneously the spectra of  $p_T$  and  $y$  can give similar pictorial representations. As we know, concrete and ready-made pictorial representations of the particle scatter plots at the stage of kinetic freeze-out given by other event generators are not available at present.

It seems that possible effects from kinematic cuts are not considered for the extracted discrete values, then for the event patterns. As we know, all the experimental data are subject to trigger and event selection restrictions, which have subsequent effects on the kinematic region in which the cross sections are defined. In fact, because our analyses are based on the experimental data themselves, the extracted parameters imply these restrictions. This renders that there are considerations on the impacts of these restrictions on the subsequent event shapes. Because the differences in experimental restrictions for  $pp$  and Pb-Pb collisions as well as for spectra of  $Z$  bosons and quarkonium states are small, the impacts on the values of parameters, discrete values, and event patterns are small in some details. Generally, these small differences in restrictions do not effect largely the global shapes and contour profiles of events.

## 4 Conclusions

We summarize here our main observations and conclusions.

(a) The transverse momentum and rapidity spectra of  $Z$  bosons produced in  $pp$  and Pb-Pb collisions at 2.76 TeV, the same spectra of charmonium  $c\bar{c}$  mesons ( $J/\psi$  and  $\psi(2S)$ ) and bottomonium  $b\bar{b}$  mesons ( $\Upsilon(1S)$ ,  $\Upsilon(2S)$ , and  $\Upsilon(3S)$ ) produced in  $pp$  collisions at 7 TeV, and the same spectra of  $J/\psi$ ,  $\Upsilon(1S)$ , and  $\Upsilon(2S)$  produced in Pb-Pb collisions at 2.76 TeV at the LHC are uniformly described by the hybrid model of two-component

Erlang distribution for  $p_T$  spectrum and the two-component Gaussian distribution for  $y$  spectrum. The former distribution results from the multisource thermal model, and the later one results from the revised Landau hydrodynamic model. The modelling results are in agreement with the experimental data measured at the LHC.

(b) In the two-component Erlang distribution Eq. (3), the first component that contributes in the low- $p_T$  region is determined by both  $m_1$  and  $\langle p_{Ti} \rangle_1$ , and the second component that contributes in the high- $p_T$  region is determined by both  $m_2$  and  $\langle p_{Ti} \rangle_2$ . The mean transverse momenta contributed by the first and second components are  $m_1 \langle p_{Ti} \rangle_1$  and  $m_2 \langle p_{Ti} \rangle_2$  respectively, and the mean transverse momentum contributed by the two components is  $\langle p_T \rangle = k_1 m_1 \langle p_{Ti} \rangle_1 + (1 - k_1) m_2 \langle p_{Ti} \rangle_2$ . Generally, we restrict  $m_1 \langle p_{Ti} \rangle_1 < m_2 \langle p_{Ti} \rangle_2$ , which ensures the first component contributing in the low- $p_T$  region and the second component contributing in the high- $p_T$  region. The two-component Gaussian function Eq. (5) is a revision of the Landau hydrodynamic model.

(c) The most important set of parameters are the mean contributions,  $\langle p_{Ti} \rangle_1$  and  $\langle p_{Ti} \rangle_2$ , of each source in the first and second components of the two-component Erlang distribution for  $p_T$  spectrum, and the peak position  $y_F$  ( $y_B$ ) and distribution width  $\sigma_{yF}$  ( $\sigma_{yB}$ ) for the forward (backward) region in the two-component Gaussian function for  $y$  spectrum. The mean contribution of each source in the two-component Erlang distribution is  $\langle p_{Ti} \rangle = \langle p_T \rangle / [k_1 m_1 + (1 - k_1) m_2]$ . From the dependences of related parameters on  $m_0$ , one can see an obvious increase in  $\langle p_{Ti} \rangle$ ,  $\langle p_{Ti} \rangle_1$ ,  $\langle p_{Ti} \rangle_2$ ,  $\langle p_T \rangle$ ,  $m_1 \langle p_{Ti} \rangle_1$ , and  $m_2 \langle p_{Ti} \rangle_2$ , and a decrease in  $y_F$  and  $\sigma_{yF}$ , when  $m_0$  changes from  $\sim 3$  GeV to  $\sim 90$  GeV. This mass scale imposes a difference on the observed data from the presence of a QCD hard scale. Because of some non-violent collision nucleons existing in the overlapping region, Pb-Pb collisions show more or less lower parameter values than  $pp$  collisions in some cases.

(d) Based on the parameter values extracted from  $p_T$  and  $y$  spectra, the event patterns (or particle scatter plots) in two-dimensional  $p_T$ - $y$  space and in three-dimensional velocity (or coordinate) space are obtained. As results of hard scattering process at the initial state, both the  $Z$  bosons and quarkonium states present some similarities and differences in event patterns. Generally,  $\sqrt{\beta_x^2} \approx \sqrt{\beta_y^2} \ll \sqrt{\beta_z^2}$ , and  $|\beta_x|_{\max} \approx |\beta_y|_{\max} < |\beta_z|_{\max}$ , which renders that the event pattern in velocity (or coordinate) space looks like a rough cylinder along the beam direction when it emits  $Z$  bosons and quarkonium states, and the maximum velocity surface is a fat cylinder which has the length being 1.2–2.2 times of diameter. The situations for  $pp$  and Pb-Pb collisions do not show an obvious difference.

(e) The cylinder diameters ( $2\sqrt{\beta_x^2}$  or  $2|\beta_x|_{\max}$ ) or lengths ( $2\sqrt{\beta_z^2}$  or  $2|\beta_z|_{\max}$ ) corresponding to emissions of charmonium  $c\bar{c}$  mesons and bottomonium  $b\bar{b}$  mesons are nearly the same. Because of large mass,  $Z$  bosons correspond to a thinner and shorter cylinder than quarkonium states in terms of  $2\sqrt{\beta_x^2}$  and  $2\sqrt{\beta_z^2}$  in velocity space, though the values of  $|\beta_z|_{\max}$  for both the types of particles are almost the same. Meanwhile, the values of  $\sqrt{y^2}$  for  $Z$  bosons are less than those for quarkonium states due to the shorter cylinder corresponding to  $Z$  bosons. The values of  $\sqrt{p_T^2}$  for  $Z$  bosons are greater than those for quarkonium states due to the excitation degree of emission sources for  $Z$  bosons being higher than that for quarkonium states. The situations for  $pp$  and Pb-Pb collisions do not show an obvious difference.

(f) The present work provides a reference in methodology which displays event patterns

(particle scatter plots) for different particles in three-dimensional velocity space or other available spaces based on the transverse momentum and rapidity spectra of considered particles. Because the present analyses are based on the experimental data themselves, the extracted parameters imply experimental restrictions. This renders that the discrete values and event patterns extracted by us are accurate to the best of our ability. It is expected that different particles correspond to different event patterns in different shapes with different sizes. To give a better comparison, the same experimental restrictions for different particles are needed in the future.

### Conflict of Interests

The authors declare that there is no conflict of interests regarding the publication of this paper.

### Acknowledgments

This work was supported by the National Natural Science Foundation of China under Grant No. 11575103 and the US DOE under contract DE-FG02-87ER40331.A008.

## References

- [1] S. S. Adler, S. A. fanasiev, C. Aidala et al. (PHENIX Collaboration), “Production of  $\phi$  mesons at midrapidity in  $\sqrt{s_{NN}} = 200$  GeV Au+Au collisions at relativistic energies,” *Physical Review C*, vol. 72, no. 1, Article ID 014903, 26 pages, 2005.
- [2] J. Adams, M. M. Aggarwal, Z. Ahammed et al. (STAR Collaboration), “ $K(892)^*$  resonance production in Au+Au and p+p collisions at  $\sqrt{s_{NN}} = 200$  GeV,” *Physical Review C*, vol. 71, no. 6, Article ID 064902, 16 pages, 2005.
- [3] I. Arsene, I. G. Bearden, D. Beavis et al. (BRAHMS Collaboration), “Quark gluon plasma and color glass condensate at RHIC? The perspective from the BRAHMS experiment,” *Nuclear Physics A*, vol. 757, nos. 1–2, pp. 1–27, 2005.
- [4] B. B. Back, M. D. Baker, M. Ballintijn et al. (PHOBOS Collaboration), “The PHOBOS perspective on discoveries at RHIC,” *Nuclear Physics A*, vol. 757, nos. 1–2, pp. 28–101, 2005.
- [5] B. Abelev, J. Adam, D. Adamová et al. (ALICE Collaboration), “Production of charged pions, kaons and protons at large transverse momenta in  $pp$  and Pb-Pb collisions at  $\sqrt{s_{NN}} = 2.76$  TeV,” *Physics Letters B*, vol. 736, pp. 196–207, 2014.
- [6] G. Aad, B. Abbott, J. Abdallah et al. (ATLAS Collaboration), “Measurement of the centrality dependence of the charged particle pseudorapidity distribution in lead-lead collisions at  $\sqrt{s_{NN}} = 2.76$  TeV with the ATLAS detector,” *Physics Letters B*, vol. 710, no. 3, pp. 363–382, 2012.

- [7] S. Chatrchyan, V. Khachatryan, A. M. Sirunyan et al. (CMS Collaboration), “Study of  $W$  boson production in PbPb and  $pp$  collisions at  $\sqrt{s_{NN}} = 2.76$ ,” *Physics Letters B*, vol. 715, nos. 1–3, pp. 66–87, 2012.
- [8] R. Aaij, B. Adeva, M. Adinolfi et al. (LHCb Collaboration), “Absolute luminosity measurements with the LHCb detector at the LHC,” *Journal of Instrumentation*, vol. 7, no. 1, Article ID P01010, 42 pages, 2012.
- [9] S. Chatterjee, S. Das, L. Kumar, D. Mishra, B. Mohanty, R. Sahoo, and N. Sharma, “Freeze-out parameters in heavy-ion collisions at AGS, SPS, RHIC, and LHC energies,” *Advances in High Energy Physics*, vol. 2015, Article ID 349013, 20 pages, 2015.
- [10] D. D. Ivanenko and D. F. Kurdgelaidze, “Hypothesis concerning quark stars,” *Astrofizika*, vol. 1, no. 4, pp. 479–482, 1965 [see also for abbreviated version, *Astrophysics*, vol. 1, no. 4, pp. 251–252, 1965].
- [11] N. Itoh, “Hydrostatic equilibrium of hypothetical quark stars,” *Progress in Theoretical Physics*, vol. 44, no. 1, pp. 291–292, 1970.
- [12] T. D. Lee and G. C. Wick, “Vacuum stability and vacuum excitation in a spin-0 field theory,” *Physical Review D*, vol. 9, no. 8, pp. 2291–2316, 1974.
- [13] Y.-H. Chen, G.-X. Zhang, and F.-H. Liu, “On productions of net-baryons in central Au-Au collisions at RHIC energies,” *Advances in High Energy Physics*, vol. 2015, Article ID 614090, 9 page, 2015.
- [14] F.-H. Liu, T. Tian, and X.-J. Wen, “Transverse mass and rapidity distributions and space dispersion plots of (net-)protons in Pb-Pb collisions at SPS energies,” *The European Physical Journal A*, vol. 50, no. 3, Article ID 50, 13 pages, 2014.
- [15] F.-H. Liu, “Dependence of charged particle pseudorapidity distributions on centrality and energy in  $p(d)A$  collisions at high energies,” *Physical Review C*, vol. 78, no. 1, Article ID 014902, 6 pages, 2008.
- [16] F.-H. Liu, “Unified description of multiplicity distributions of final-state particles produced in collisions at high energies,” *Nuclear Physics A*, vol. 810, nos. 1–4, pp. 159–172, 2008.
- [17] F.-H. Liu, Y.-Q. Gao, T. Tian, and B.-C. Li, “Unified description of transverse momentum spectrums contributed by soft and hard processes in high-energy nuclear collisions,” *The European Physical Journal A*, vol. 50, no. 6, Article ID 94, 9 pages, 2014.
- [18] L. D. Landau, “Izvestiya akademii nauk: series fizicheskikh 17 51 (1953),” in *English-Translation: Collected Papers of L. D. Landau*, D. Ter-Haarp, Ed., p. 569, Pergamon, Oxford, UK, 1965.

- [19] S. Z. Belenkij and L. D. Landau, “Soviet Physics Uspekhi 56 309 (1955),” in *English-Translation: Collected Papers of L.D. Landau*, D. Ter-Haarp, Ed., p. 665, Pergamon, Oxford, UK, 1965.
- [20] P. A. Steinberg, “Bulk dynamics in heavy ion collisions,” *Nuclear Physics A*, vol. 752, nos. 1–4, pp. 423–432, 2005.
- [21] P. Carruthers and M. Duong-Van, “Rapidity and angular distributions of charged secondaries according to the hydrodynamical model of particle production,” *Physical Review D*, vol. 8, no. 3, pp. 859–874, 1973.
- [22] E. V. Shuryak, “Multiparticle production in high energy particle collisions,” *Yadernaya Fizika*, vol. 16, no. 2, pp. 395–405, 1972.
- [23] P. Carruthers, “Heretical models of particle production,” *Annals of the New York Academy of Sciences*, vol. 229, no. 1, pp. 91–123, 1974.
- [24] O. V. Zhirov and E. V. Shuryak, “Multiple production of hadrons and predictions of the Landau theory,” *Yadernaya Fizika*, vol. 21, pp. 861–867, 1975.
- [25] M. Gazdzicki, M. Gorenstein, and P. Seyboth, “Onset of deconfinement in nucleus-nucleus collisions: review for pedestrians and experts,” *Acta Physica Polonica B*, vol. 42, no. 2, pp. 307–351, 2011.
- [26] Z. J. Jiang, H. P. Deng, Y. Zhang, and H. L. Zhang, “Unified descriptions of Hwa-Bjorken and Landau relativistic hydrodynamics and the pseudorapidity distributions in high energy heavy ion collisions,” *Nuclear Physics Review (China)*, vol. 32, no. 4, pp. 398–404, 2015.
- [27] S. Chatrchyan, V. Khachatryan, A.M. Sirunyan et al. (CMS Collaboration), “Study of  $Z$  production in PbPb and  $pp$  collisions at  $\sqrt{s_{NN}} = 2.76$  TeV in the dimuon and dielectron decay channels,” *Journal of High Energy Physics*, vol. 2015, no. 3, Article ID 22, 40 pages, 2015.
- [28] G. Aad, T. Abajyan, B. Abbott et al. (ATLAS Collaboration), “Measurement of  $Z$  boson production in Pb-Pb collisions at  $\sqrt{s} = 2.76$  TeV with the ATLAS Detector,” *Physical Review Letters*, vol. 110, no. 2, Article ID 022310, 18 pages, 2013.
- [29] G. Aad, B. Abbott, J. Abdallah et al. (ATLAS Collaboration), “Measurement of the centrality dependence of  $J/\psi$  yields and observation of  $Z$  production in lead-lead collisions with the ATLAS detector at the LHC,” *Physics Letters B*, vol. 697, no. 4, pp. 294–312, 2011.
- [30] B. Abelev, J. Adam, D. Adamová et al. (ALICE Collaboration), “Measurement of quarkonium production at forward rapidity in  $pp$  collisions at  $\sqrt{s} = 7$  TeV,” *The European Physical Journal C*, vol. 74, no. 8, Article ID 2974, 21 pages, 2014.
- [31] K. Aamodt, A. A. Quintana, D. Adamová et al. (ALICE Collaboration), “Rapidity and transverse momentum dependence of inclusive  $J/\psi$  production in  $pp$  collisions at  $\sqrt{s} = 7$  TeV,” *Physics Letters B*, vol. 704, no. 5, pp. 442–455, 2011.

- [32] K. Aamodt, A. A. Quintana, D. Adamová et al. (ALICE Collaboration), “Erratum to ‘Rapidity and transverse momentum dependence of inclusive  $J/\psi$  production in  $pp$  collisions at  $\sqrt{s} = 7$  TeV’ [Phys. Lett. B 704 (5) (2011) 442],” *Physics Letters B*, vol. 718, no. 2, pp. 692–698, 2012.
- [33] R. Aaij, B. Adeva, M. Adinolfi et al. (LHCb Collaboration), “Measurement of  $J/\psi$  production in  $pp$  collisions at  $\sqrt{s} = 7$  TeV,” *The European Physical Journal C*, vol. 71, no. 5, Article ID 1645, 17 pages, 2011.
- [34] R. Aaij, C. A. Beteta, B. Adeva et al. (LHCb Collaboration), “Measurement of  $\psi(2S)$  meson production in  $pp$  collisions at  $\sqrt{s} = 7$  TeV,” *The European Physical Journal C*, vol. 72, no. 8, Article ID 2100, 12 pages, 2012.
- [35] R. Aaij, C. A. Beteta, B. Adeva et al. (LHCb Collaboration), “Measurement of  $\Upsilon$  production in  $pp$  collisions at  $\sqrt{s} = 7$  TeV,” *The European Physical Journal C*, vol. 72, no. 6, Article ID 2025, 12 pages, 2012.
- [36] S. Chatrchyan, V. Khachatryan, A. M. Sirunyan et al. (CMS Collaboration), “Measurement of the  $\Upsilon(1S)$ ,  $\Upsilon(2S)$ , and  $\Upsilon(3S)$  cross sections in  $pp$  collisions at  $\sqrt{s} = 7$  TeV,” *Physics Letters B*, vol. 727, nos. 1-3, pp. 101–125, 2013.
- [37] V. Khachatryan, A. M. Sirunyan, A. Tumasyan et al. (CMS Collaboration), “Upsilon production cross section in  $pp$  collisions at  $\sqrt{s} = 7$  TeV,” *Physical Review D*, vol. 83, no. 11, Article ID 112004, 27 pages, 2011.
- [38] J. Adam, D. Adamová M.M. Aggarwal et al. (ALICE Collaboration), “Differential studies of inclusive  $J/\psi$  and  $\psi(2S)$  production at forward rapidity in Pb-Pb collisions at  $\sqrt{s_{NN}} = 2.76$  TeV,” *Journal of High Energy Physics*, vol. 2016, no. 05, Article ID 179, 48 pages, 2016.
- [39] S. Chatrchyan, V. Khachatryan, A. M. Sirunyan et al. (CMS Collaboration), “Suppression of non-prompt  $J/\psi$ , prompt  $J/\psi$ , and  $\Upsilon(1S)$  in PbPb collisions at  $\sqrt{s_{NN}} = 2.76$  TeV,” *Journal of High Energy Physics*, vol. 2012, no. 05, Article ID 063, 54 pages, 2012.
- [40] The CMS Collaboration, “Suppression of  $\Upsilon(1S)$ ,  $\Upsilon(2S)$  and  $\Upsilon(3S)$  in PbPb collisions at  $\sqrt{s_{NN}} = 2.76$  TeV,” *CMS Physics Analysis Summary*, preprint CMS PAS HIN-15-001, Available on the CERN CDS information server, 2015, <http://cds.cern.ch/record/2030083/files/HIN-15-001-pas.pdf>, 2015.
- [41] G. D. Lafferty, T. R. Wyatt, “Where to stick your data points: The treatment of measurements within wide bins,” *Nuclear Instruments and Methods in Physics Research A*, vol. 355, nos. 2–3, pp. 541–547, 1995.